UCLA
UCLA Previously Published Works

Title

Distilling the Evolving Contributions of Anthropogenic Aerosols and Greenhouse Gases to Large-Scale Low-Frequency Surface Ocean Changes Over the Past Century

Permalink

Journal

ISSN

Authors

Dong, Yue
Kay, Jennifer E
Deser, Clara
et al.

Publication Date

DOI

Copyright Information

Peer reviewed

Distilling the Evolving Contributions of Anthropogenic Aerosols and Greenhouse Gases to Large-Scale Low-Frequency Surface Ocean Changes Over the Past Century

Yue Dong[1,2] ![ORCID], Jennifer E. Kay[1,3] ![ORCID], Clara Deser[4], Antonietta Capotondi[1,5] ![ORCID], and Sara C. Sanchez[3] ![ORCID]

[1]Cooperative Institute for Research in Environmental Sciences, University of Colorado Boulder, Boulder, CO, USA, [2]Department of Atmospheric and Oceanic Sciences, University of California Los Angeles, Los Angeles, CA, USA, [3]Department of Atmospheric and Oceanic Sciences, University of Colorado Boulder, Boulder, CO, USA, [4]Climate and Global Dynamics Division, NCAR, Boulder, CO, USA, [5]Physical Sciences Laboratory, NOAA, Boulder, CO, USA

Abstract Anthropogenic aerosols (AER) and greenhouse gases (GHG)—the leading drivers of the forced historical change—produce different large-scale climate response patterns, with correlations trending from negative to positive over the past century. To understand what caused the time-evolving comparison between GHG and AER response patterns, we apply a low-frequency component analysis to historical surface ocean changes from CESM1 single-forcing large-ensemble simulations. While GHG response is characterized by its first leading mode, AER response consists of two distinct modes. The first one, featuring long-term global AER increase and global cooling, opposes GHG response patterns up to the mid-twentieth century. The second one, featuring multidecadal variations in AER distributions and interhemispheric asymmetric surface ocean changes, appears to reinforce the GHG warming effect over recent decades. AER thus can have both competing and synergistic effects with GHG as their emissions change temporally and spatially.

Plain Language Summary Anthropogenically forced climate change over the past century has been mainly caused by two types of emissions: greenhouse gases (GHG) and aerosols (AER). In general, sulfate aerosols from industrial sources can reflect shortwave radiation to yield a cooling effect opposite to the GHG warming effect. However, model simulations isolating GHG and AER forcings show that the large-scale climate effect of AER does not always dampen the GHG effect. Instead, over recent decades, AER have produced surface ocean response patterns more like the GHG response. Using a novel low-frequency statistical decomposion, we find that aerosols have driven two distinct modes of climate change patterns over the historical period. The first mode is associated with global aerosol increase, resulting in global-wide cooling damping the GHG-induced warming. The second mode is associated with the shift in aerosol emissions from north America/western Europe to southeast Asia, which drives regional changes enhancing the GHG effect. Our results highlight the importance of considering the temporal and spatial evolutions of AER emissions in assessing GHG and AER climate effects and attributing historical anthropogenic climate changes to GHG and AER forcings.

1. Introduction

Anthropogenically forced climate change over the past century has been primarily driven by two components: greenhouse gases (GHG) and anthropogenic aerosols (AER). These components modulate the global-mean surface temperature through distinct radiative effects (Forster et al., 2021; Myhre et al., 2014): GHG cause surface warming due to absorption and re-emission of longwave radiation, while AER change energy budget through reflection or absorption of shortwave radiation by scattering (e.g., sulfate) or absorbing (e.g., black carbon) species. Additionally, AER have indirect effects on climate through cloud-aerosol interactions, where aerosols can serve as cloud condensation nuclei affecting clouds' albedo, lifetime, and properties (Ackerman et al., 2004; Twomey, 1977). Over the past century, long-term increases in global-mean GHG and AER have led to a large cancellation between GHG-induced warming and AER-induced cooling effects (Deser et al., 2020a).

While a clear opposing effect from GHG and AER on global-mean surface temperature has been found, comparing the spatial patterns of their climate responses has been less straightforward. Focusing on global GHG and AER forcings in the twentieth century, Xie et al. (2013) found that the first leading modes of climate response patterns to GHG and AER bear a great resemblance, suggesting that large-scale climate responses are governed by

the same ocean-atmosphere feedbacks intrinsic to the climate system. Wang et al. (2016) further examined the differences in those leading modes, highlighting the unique features of AER forced response associated with interhemispheric temperature asymmetry and cross-equatorial circulation change.

The spatial distributions of GHG and AER forcings add additional complexity to the comparison. Unlike well-mixed GHG, AER emissions have much richer structures in their spatial distributions and temporal evolution (Deser et al., 2020a). Emissions from North America (NA) and western Europe (EU) have dominated the global total AER loading since the early decades of the twentieth century until the 1970s, after which they have declined substantially following emission regulations. On the other hand, emissions from southeast Asia (SA) have been increasing gradually since the 1950s, and more recently, have surpassed the emissions from NA and EU since the 1990s. This transition of major AER sources has been identified as an AER "shift" mode, causing various climate changes in a different way than global-mean AER changes, ranging from large-scale SST patterns and ocean meridional overturning circulations (Kang et al., 2021; Shi et al., 2022) to the seasonal cycle of regional precipitation (Dong et al., 2024; Song et al., 2021). A thorough comparison between the two distinct modes of aerosol forcing has been discussed in Shi et al. (2022), where they found the shift mode can compensate for the global-mean AER effect. However, a key question left unanswered is: how do these different AER modes affect the time-evolving AER forced response, the comparison between GHG and AER effects, and ultimately, the respective contributions of GHG and AER to transient historical climate change?

To review the literature and to illustrate the evolving contributions of GHG and AER to forced historical trends, we begin by showing the ensemble-mean response of CESM1 single-forcing large-ensemble (SF-LE) simulations (Deser et al., 2020a). Figure 1 shows the trend patterns for sea-surface temperature (SST) and sea-surface salinity (SSS), and key atmospheric variables coupled with them, sea level pressure (SLP) and surface water fluxes (i.e., precipitation minus evaporation, P-E). We compare these trend patterns forced by all forcings ("ALL"; from the CESM1 LE project, Kay et al., 2015, 2015), GHG, and AER single-forcing simulations (from Deser et al., 2020b). As found in previous studies, during the early period (1940–1980; Figure 1a), the total forced response is dominated by AER, featuring an inter-hemispheric contrast with pronounced cooling due to the SW absorption by AER and salinification trends in the northern hemisphere (NH) driven by an enhancement of Atlantic Meridional Overturning Circulation (AMOC; Menary et al., 2020) and increased sea-ice formation in the Arctic ocean. During recent decades (1980–2020; Figure 1b), the total forced response has been dominated by GHG, featuring broad global warming, a "wet-get-wetter" precipitation pattern, and a "salty-get-saltier" SSS pattern, consistent with the literature (Capotondi et al., 2012; Durack et al., 2012; Held & Soden, 2006; Xie et al., 2010).

Perhaps more interestingly, the climate response patterns driven by GHG and AER largely oppose each other during the early period, but show some resemblance during the later period at regional scales (e.g., NH warming and Arctic freshening). We further compute the pattern correlations for running 40-year trends in global SST and SSS between the ALL and single forcing (GHG or AER) ensemble-means, following Deser et al. (2020). As expected, the pattern correlations between ALL and GHG for both SST and SSS have increased steadily since the 1950s (red lines in Figures 1c and 1d), suggesting the increasingly dominant role of GHG in modulating global climate. However, the pattern correlations between ALL and AER decreased only over the first half of the twentieth century and have gradually rebounded over recent decades (blue lines in Figures 1c and 1d). The same non-monotonic behavior is also found for the pattern correlation between GHG and AER (black lines in Figures 1c and 1d), indicating that the surface ocean response patterns to AER have become closer, not opposite, to those forced by GHG over recent decades.

This comparison between the evolving AER and GHG forced responses led us to ask: what caused the AER response to change over time, and particularly, to amplify the GHG response over recent decades? Is it because of the decline of global AER emissions, or is it because of the change in the spatial distribution of those emissions, or both? And what implications does this have for detecting and attributing historical low-frequency surface ocean changes? To address these important but previously unanswered questions, we distill the leading modes of low-frequency historical surface ocean changes driven by GHG and AER, quantify the relative roles of each mode, and ultimately, synthesize the evolving contributions of GHG and AER responses to historical forced climate change.

2. Low-Frequency Component Anlaysis

One of the caveats in the trend pattern analysis in Figure 1 and other studies (Deser et al., 2020a; Kang et al., 2021; Wang & Wen, 2022) is that these trends are computed over specific time intervals, thus may not
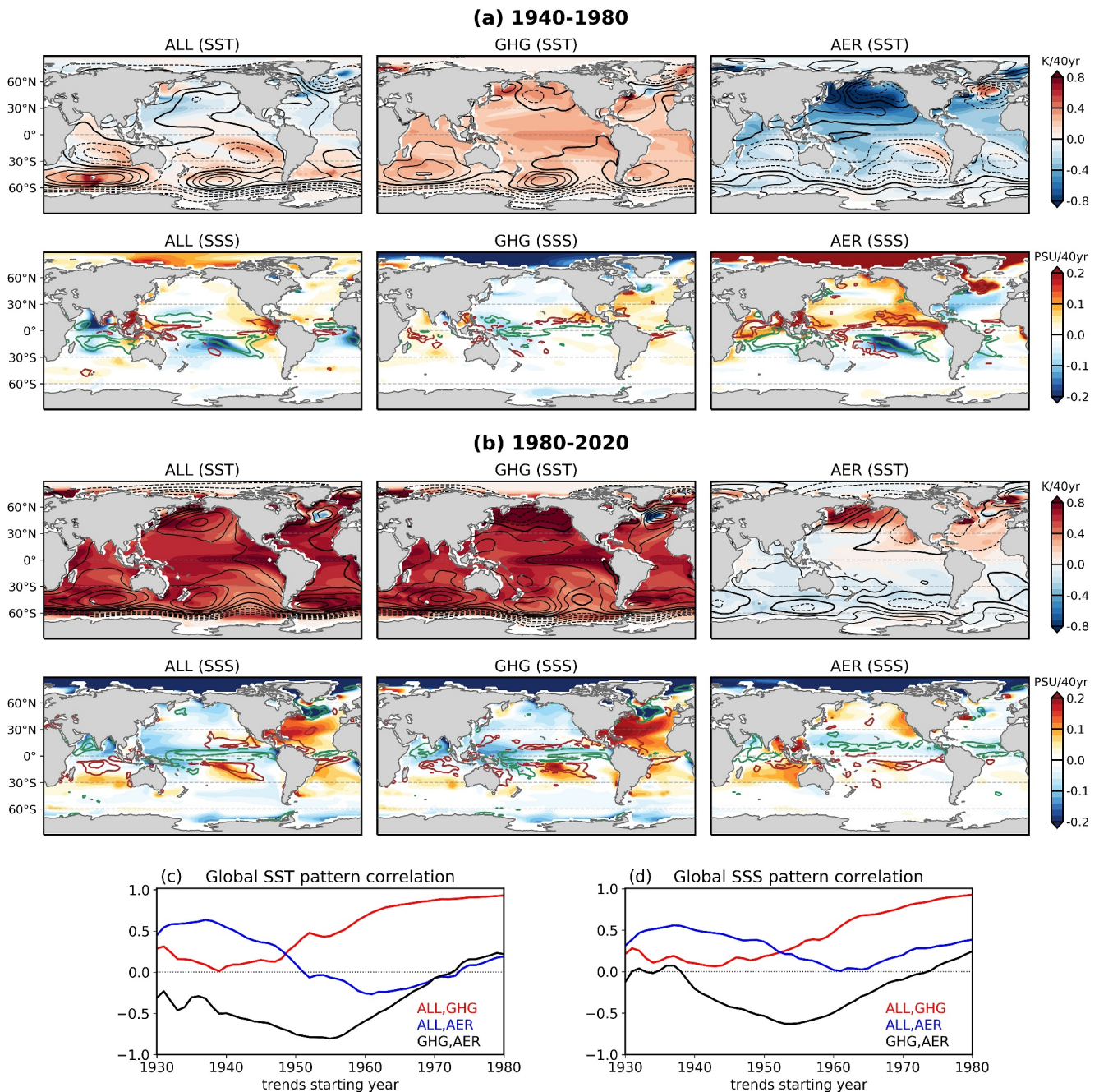
Figure 1. CESM1 ensemble-mean trend response to ALL, GHG and AER forcings, for (a) 1940–1980 and (b) 1980–2020. Black contours overlaid on the SST panels are SLP trends (contour interval is 0.16 hPa/40 yr, zero contours are thickened, solid contours denote positive SLP trend, dashed contours denote negative SLP trend). Colored contours overlaid on the SSS panels are P-E trends (contour interval is 0.18 mm/day/40 yr, zero contours are omitted; green denotes positive P-E and red denotes negative P-E) (c), (d) Pattern correlations for 40-year running trends in ensemble-mean (d) global SST and (e) global SSS between ALL, GHG and AER.

capture the whole series of the forced response and time-evolving forcing patterns. To achieve a more systematic assessment, other prior studies have utilized principal component (PC) analysis to linearly separate the total response into several empirical orthogonal functions (EOFs) (e.g., Bonfils et al., 2020; Wang et al., 2016; Xie et al., 2013). However, the EOF results can be affected by high-frequency natural variability (e.g., ENSO) that is not completely removed due to insufficient ensemble size. While a previous study (Wang & Wen, 2022) addressed this by using a low-pass filtered EOF analysis, here we employ a novel statistical approach, low-frequency component analysis (LFCA; Wills et al., 2018), to robustly examine the *low-*

frequency forced response in CESM1 LE. In the following sections, we first introduce the LFCA method and the data analyzed (Section 2.1), and we next show the results of the leading low-frequency modes for the GHG and AER forced response (Section 2.2).

2.1. The LFCA Method and Data

Unlike the conventional PC analysis which maximizes total variance, LFCA finds a linear combination of EOFs that maximize the ratio of low-pass filtered variance to total variance, thereby isolating the leading modes of low-frequency variability (Wills et al., 2018a). Previous studies (Dörr et al., 2023; Wills et al., 2022) further suggest that applying LFCA to multiple spatial-temporal fields jointly to account for the leading low-frequency in separate fields can improve the isolation of long-term forced response.

Therefore, in this study we perform joint LFCA on global annual-mean SST and SSS anomalies over 1921–2020 to study low-frequency modes of forced historical surface ocean changes. The anomalies are relative to the 1921–2020 climatology. We take the SST and SSS response from the ensemble-mean of ALL, GHG and AER ensembles as part of CESM1 SF-LE (Deser et al., 2020a), each containing 20 members. We also note that in this set of LEs, AER specifically refers to industrial aerosols, not including biomass aerosols.

For the joint LFCA, we use a 15-year cut-off low-pass filter to isolate multidecadal low-frequency variability, and we retain the 10 leading EOFs, which in total account for 99.9%, 99% and 97% of the joint low-frequency variance for ALL, GHG and AER, respectively. Additionally, to understand the dynamical processes associated with each mode, we regress annual-mean SLP, precipitation (P), evaporation (E) and P-E anomalies onto the timeseries of each of the PCs.

Although we take the ensemble mean response first to remove random internal variability before performing the joint LFCA, one can also perform LFCA on each ensemble member to obtain (the best estimate of) its low-frequency forced response and then average the leading modes across ensemble members (e.g., Kuo et al., 2023; Wills et al., 2022). We will show in the next section that the results remain the same regardless of which method is used (cf. Figure 2 and Figure S1 in Supporting Information S1). Additionally, conducting the LFCA based on seasonal mean quantities does not show significant differences from annual-mean results (cf. Figure 2 and Figures S2, S3 in Supporting Information S1).

2.2. Low-Frequency Modes of GHG and AER Forced Responses

Figure 2 shows the leading joint LFCA modes of SST and SSS for the GHG and AER forced responses. The GHG forced response is dominated by a single mode that explains 97.2% of the low-frequency variance; we will denote its timeseries as "GHG PC1" hereafter. The AER forced response consists of two leading modes, which both have strong multi-decadal variability and explain 75.4% and 12.7% of the total low-frequency variance, respectively. We will denote their timeseries as "AER PC1" and "AER PC2" hereafter.

The GHG PC1 has increased monotonically throughout the past century, with a pronounced positive trend starting from 1980 (Figure 2a). The corresponding SST pattern is characterized by broad global warming and enhanced tropical eastern Pacific warming (i.e., the El Niño-like SST pattern), accompanied by a reduced tropical zonal SLP gradient (Figure 2b). The global-scale warming causes precipitation to increase in the tropics and decrease in the broad subtropics (Figure S4a in Supporting Information S1), following the "wet-get-wetter" and "warmer get wetter" mechanism (Held & Soden, 2006; Xie et al., 2010). Associated with enhanced global-scale evaporation (Figure S4b in Supporting Information S1), the net P-E pattern links to a "salty-get-saltier" SSS pattern (Figure 2c Durack et al., 2012; Sun et al., 2021), with an enhanced SSS gradient between tropical and subtropical oceans as well as an amplified climatological contrast between the Pacific and Atlantic basins.

On the other hand, AER PC1 and PC2 feature distinct surface ocean patterns and time evolutions (Figures 2d–2k). By regressing aerosol optical depth (AOD) onto PC1 and PC2, we find that the first mode is associated with a globally increasing AOD pattern, with the largest source in east Asia (Figure 2g). The positive AOD anomalies cause global-scale SST cooling by reflecting SW radiation, which is most pronounced in the north Pacific downstream of the east Asian AOD source (Figure 2e). The AOD-induced surface cooling further reduces precipitation in east Asia extending to the north Pacific (Figure S4c in Supporting Information S1), along with the weakly decreased evaporation (Figure S4d in Supporting Information S1), leading to increased SSS in the north Pacific (Figure 2f). Additionally, global cooling increases Arctic sea-ice cover, thereby increasing its SSS (Figure
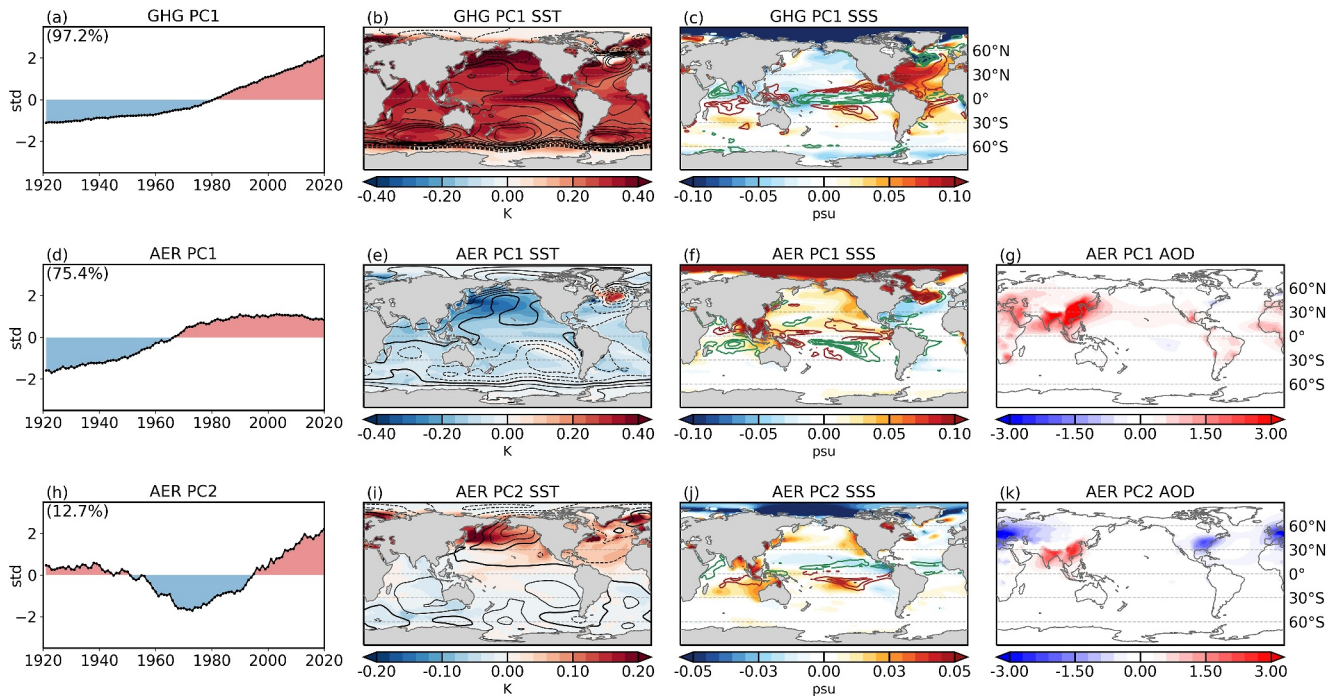
Figure 2. Leading low-frequency modes of GHG and AER ensemble-mean responses obtained from joint SST/SSS LFCA. (a, d, h) Leading PCs; (b, e, i) corresponding SST patterns and (c, f, j) corresponding SSS patterns. Numbers in the corner of the timeseries plots show the low-frequency variance explained by the corresponding PC. SLP regressions are overlaid on the SST patterns (contour interval is 0.05 hPa, zero contours are thickened, solid contours denote positive SLP and dashed contours denote negative SLP); P-E regressions are overlaid on the SSS patterns (interval is 0.06 mm/day, zero contours are omitted, green denotes positive P-E and red denotes negative P-E). (g, k) Regressions of aerosol optical depth at the 550 nm (no unit, multiplied by 100) onto AER PC1 and PC2.

S5 in Supporting Information S1). Overall, AER PC1 increases through most of the twentieth century, with the strongest positive trend from 1940 to 1980 and a negligible trend after 1980 (Figure 2d).

By contrast, AER PC2 is associated with the relative difference in AOD between northeast America/western Europe and southeast Asia (Figure 2k). This PC has a negative trend from the early twentieth century to 1970 and a reversed (positive) trend from 1980 to present day (Figure 2h), reflecting the transition of major AER emissions from NA/EU to SA over the course of the twentieth century. In the positive phase of PC2, the negative AOD in NA/EU drives NH surface warming confined to mid-to-high latitudes (Figure 2i) and Arctic freshening via increased runoff from sea-ice melting (Figure 2j; Figure S5 in Supporting Information S1). The positive AOD in SA drives weak cooling (Figure 2i) and drying locally in the Indo-Pacific ocean (Figure S1e in Supporting Information S1), which excites a Rossby wave response weakening the Aleutian Low (Figure 2i; also see Smith et al. (2016); Dittus et al. (2021)). Due to the zonal-mean energy budget constraint, the ITCZ shifts northward toward the warmer NH as required by cross-equatorial heat transport (Hwang et al., 2013; Kang et al., 2008), resulting in enhanced precipitation north of the equator and reduced precipitation in the south (Figure S4e in Supporting Information S1). This zonal-mean precipitation dipole pattern further links to a meridional SSS gradient in the tropical Pacific, with decreased (increased) SSS in the north (south) (Figure 2j).

In summary, the leading low-frequency modes of GHG and AER forced responses are diverse in both their spatial patterns and temporal evolutions. The GHG response can be largely captured by a single leading mode, which has increased monotonically throughout the past century. The AER forced response, however, features two distinct modes. AER PC1 is associated with increasing global AER emissions and resulting global cooling as well as enhanced regional responses in the NH western Pacific associated with east Asian emissions. AER PC2 represents a multidecadal variation in AER distribution from high-latitude NA/EU to low-latitude SA over recent decades. This zonally asymmetric AER forcing, however, yields an inter-hemispheric SST gradient and a shift in zonal-mean precipitation and SSS anomalies.
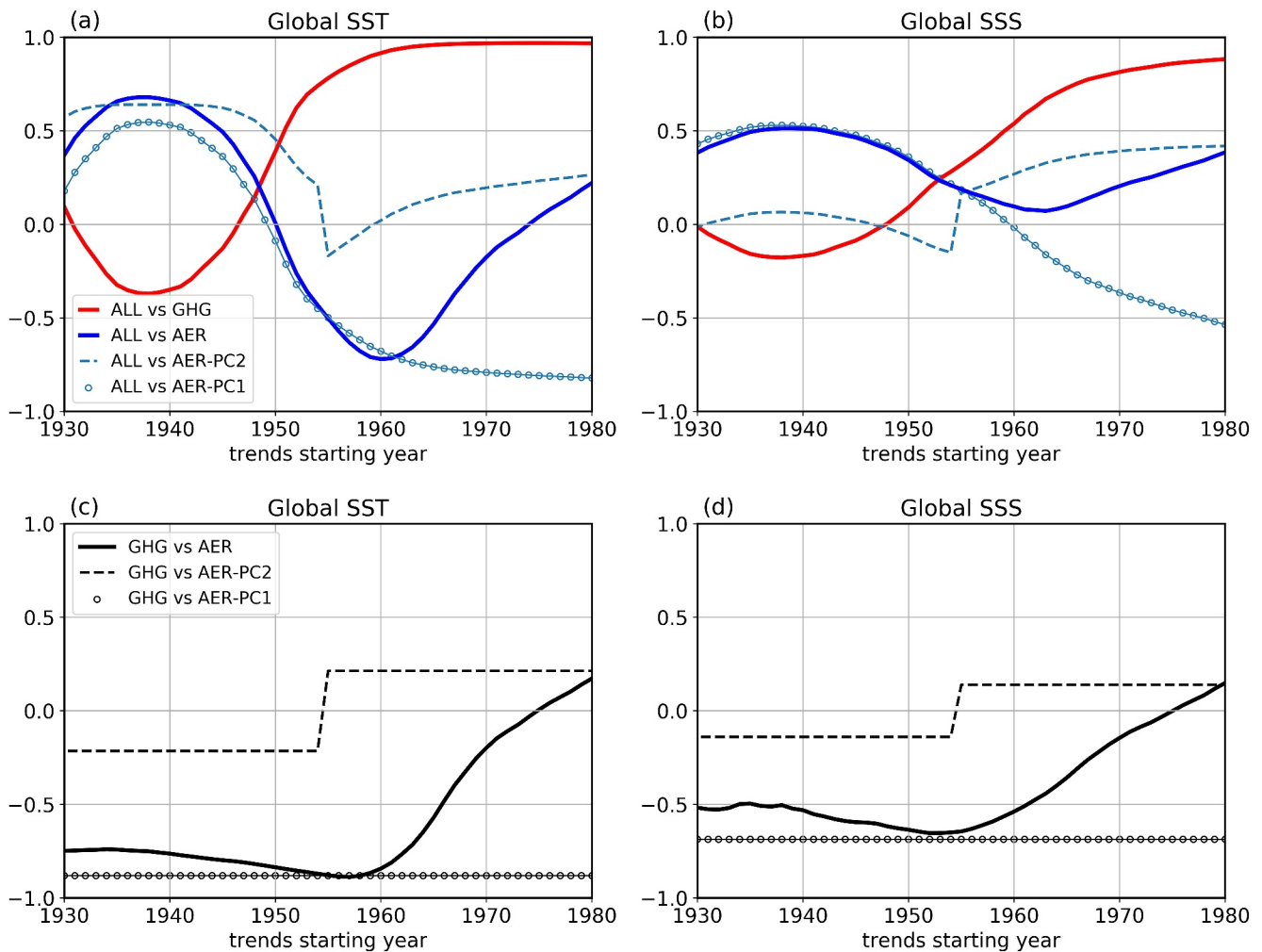
Figure 3. Pattern correlations for running 40-year trends in (left) global SST and global SSS (right) response reconstructed using the LFCA leading modes, between (a, b) ALL and GHG or AER responses and (c, d) between GHG and AER responses. Note that the x-axis shows the starting year of the running 40-year trend period.

3. Time-Evolving Contributions of the Leading Modes of AER and GHG Responses

Having shown the leading modes of AER and GHG responses, in this section, we focus on running pattern correlations to quantify the evolving roles of each individual mode to the total forced response.

First, we approximate the time-varying forced responses using their leading LFCA modes, and repeat the pattern correlation analysis for running 40-year trends in global SST and SSS as in Figure 1 but use the PC-reconstructed responses. We find that using the first leading mode for GHG response and the leading two modes for AER and ALL response can faithfully reproduce the results of the simulated total response (cf. Figures 1c and 1d, 3). The PC-based pattern correlations capture the increasingly high values between ALL and GHG (red solid lines) and the non-monotonic evolution of the correlations between ALL and AER (blue solid lines) and between GHG and AER (black solid lines) for both SST and SSS trend patterns.

Having verified that the LFCA modes can sufficiently reproduce the total response, now we come back to the questions raised at the beginning: what caused the AER response to change over time and to amplify (rather than offset) the GHG response over recent decades? More specifically, is it because of the change in AER PC1 associated with global AER emissions or the change in PC2 associated with shifting AER emissions, or both?

To answer these questions, we repeat the pattern correlation analysis with individual AER PCs. When only accounting for AER PC1, the trend pattern correlations between ALL and AER decrease monotonically after the 1940s (Figures 3a and 3b, blue circled lines), unlike the total AER response which bounces back after the 1960s

(blue solid lines). Furthermore, the pattern correlations between AER PC1 and GHG PC1 stay at a constant negative value of −0.88 for SST and −0.69 for SSS (Figures 3c and 3d, black circled lines), indicating that the response patterns associated with AER PC1 have continuously opposed those driven by GHG PC1. The high (albeit negative) pattern correlations between GHG PC1 and AER PC1 can already be seen in Figure 2: both modes feature a global-wide SST response driven by global forcing (with sign reversed), and a similar hydrological cycle response constrained by global warming or cooling, all consistent with earlier findings by Xie et al. (2013).

Turning to AER PC2, although this mode has a much weaker pattern correlation with GHG PC1 overall, the correlation switches sign from negative to positive around mid-century (Figures 3c and 3d, black dashed lines), suggesting that it is AER PC2, not PC1, that makes the total AER forced response patterns more similar to the GHG response patterns (Figures 3c and 3d, black solid lines). The abrupt change in the running trend pattern correlations arises from the phase transition in the AER PC2 timeseries around the 1980s associated with the shift in major AER emissions from NA/EU to SA. As AER emissions increase over SA and decrease over NA/EU after the 1980s, this mode produce north Pacific warming, Arctic freshening and SH subtropical drying, similar to the GHG-induced local changes (Figure 2). Although it also yields regional changes that are different from the GHG response (e.g., SST in the tropical Pacific), its global pattern correlations with GHG PC1 shows that the transition in this shift mode has driven the overall AER-forced response from opposing to resembling the GHG response.

To further illustrate the different contributions of AER PC1 and PC2 to the total forced response, we show the trend patterns for AER and GHG PCs. Figures S6 and S7 in Supporting Information S1 show that AER emissions and the forced trend responses to those emissions over 1940–1980 arise primarily from PC1 (Figure S6a in Supporting Information S1) and over 1980–2020 arise nearly entirely from PC2 (Figure S6b in Supporting Information S1). Moreover, the increase in global-mean AOD from the early twentieth century to the 1980s is predominately associated with PC1 and the moderate decline in global AOD afterward is caused mainly by PC2 (Figure S8 in Supporting Information S1).

Overall, these findings suggest that both PC1 and PC2 make significant contributions to the AER response, but their roles vary in time. Over the first half of the twentieth century until the 1980s, PC1 dominates the total AER forcing and the forced response (Figures S6, S7 in Supporting Information S1), with patterns largely *opposite* to those of GHG (Figures 3c and 3d). If the spatial pattern of AER emissions had remained unchanged from that of PC1 but continued to increase in magnitude over the past 40 years, the GHG response would have been largely compensated for by AER, resulting in a less detectable anthropogenically forced signal over the past century. However, the geographical distribution of AER emissions did change, shifting from NA/EU to SA, which led to the prominent phase transition in PC2 over recent decades. Although PC2 is associated with small global-mean AOD anomalies (Figure S8 in Supporting Information S1), the dynamical response associated with this AER shift mode can be large at regional scales (Figure S6 in Supporting Information S1). Some of the regional responses appear to *enhance* the GHG-induced changes, leading to a synergistic effect of AER with GHG over recent decades rather than a competing effect as in earlier periods.

4. Implications for Detection and Attribution

The time-evolving similarities and disparities between GHG and AER forced responses have important implications for detecting and attributing (D&A) historical climate change. Previous D&A studies, for example, Bonfils et al. (2020), used an EOF approach with historical simulations and identified two externally forced fingerprints. They argued that the first one, featuring global warming and intensified wet-dry patterns, is driven by GHG, and that the second one, featuring an inter-hemispheric temperature contrast and meridional shift in ITCZ location, is driven by AER.

Using the SST/SSS joint LFCA, we also find two leading modes in the CESM1 ALL ensemble-mean response (Figure 4), similar to the results of Bonfils et al. (2020). Indeed, at first glance, ALL PC1 and PC2 seem to bear a strong resemblance to GHG PC1 and AER PC1, respectively (Figure 2). However, there are substantial differences between the patterns of ALL PC1 and GHG PC1. For example, GHG PC1 is characterized by a strong El Niño-like SST warming pattern (Figure 2b), a zonal-mean wet-dry hydrological pattern (Figure S4a in Supporting Information S1) and a corresponding zonal-mean SSS pattern in the Pacific (Figure 2c). By contrast, ALL PC1 has a more uniform tropical SST pattern (Figure 4b), a zonally asymmetric precipitation pattern with drying in the west Pacific and wetting in the central Pacific (Figure S9a in Supporting Information S1), and a resulting SSS
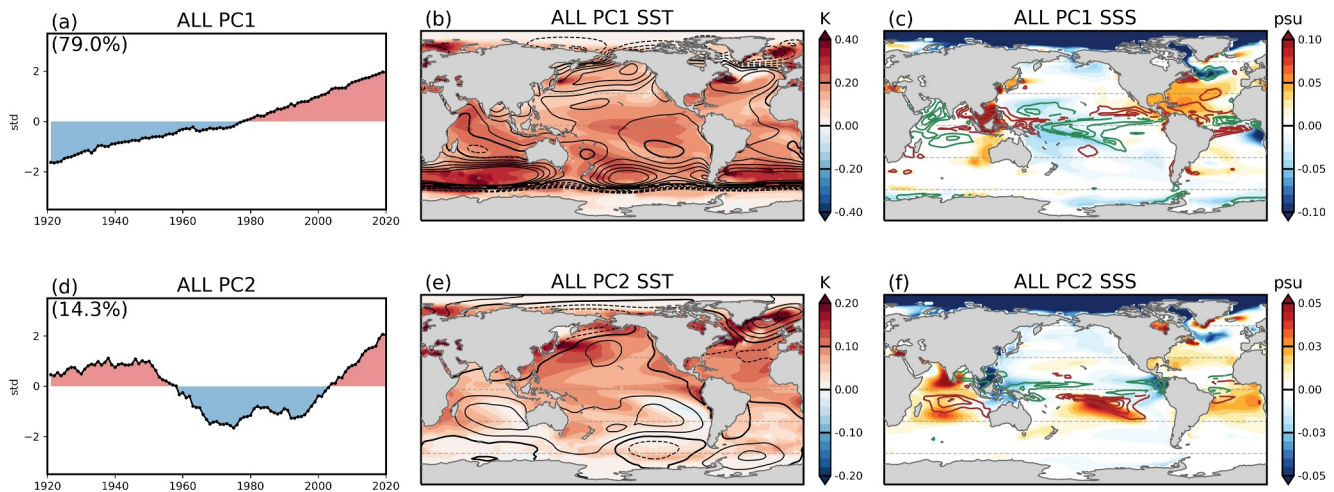
Figure 4. Same with Figure 1, except for the two leading modes obtained from CESM1 ALL ensemble-mean responses.

dipole pattern in the western Pacific (Figure 4e). These mismatches, however, appear to be consistent with AER PC1, with a high pattern correlation of −0.7 for global SST between ALL PC1 (Figure 4b) and AER PC1 (Figure 2e). Similarly, while the response patterns of ALL PC2 are overall anti-correlated with AER PC1, there are noticeable spatial features that cannot be explained by AER PCs but rather resemble GHG PC1. Collectively, this suggests that the two modes of historical anthropogenic fingerprints obtained from CESM1 ALL simulations are forced by the combined effects of GHG and AER, rather than by each forcing agent individually as previously proposed (Bonfils et al., 2020).

Thus, we argue that previous D&A approaches that separate the leading modes of historical fingerprints to GHG and AER may be biased, as they don't account for the two distinct modes of AER response and their evolving synergistic and competing climate effects with GHG. Our CESM1 results suggest that robustly detecting and attributing historical forced climate change requires careful separation of GHG and AER responses, which are not mutually independent.

5. Summary

By leveraging a novel low-frequency component analysis and running pattern correlation analysis, we have distilled the leading modes of low-frequency climate responses to GHG and AER forcing, and for the first time, quantified the evolving roles of individual AER modes in the context of transient historical climate change. While the GHG response can be well represented by a single dominant mode, the AER response features two distinct modes. The first mode (PC1) is associated with an increase in global AER emissions over the past century, driving global-wide cooling and regional "wet-get-wetter" precipitation and "salty-get-saltier" salinity response patterns. This AER mode is spatially anti-correlated with the leading GHG mode and is the main contributor to the negative correlations between GHG and AER response patterns throughout the first half of the twentieth century. However, such a GHG-damping effect by AER has stopped and reversed sign, leaving an increasingly positive correlation between GHG and AER response trend patterns in recent decades. We find this is not due to global-mean AER decrease from the first mode, but due to the geographic redistribution of AER emissions - the second mode (PC2) - associated with the recent shift from north America/western Europe to southeast Asia emissions. This AER shift mode features a meridional dipole pattern of zonal-mean surface ocean and hydrological responses, and causes NH high-latitude warming anomalies that enhance, rather than offset, the GHG-induced changes.

Furthermore, by comparing the leading modes of GHG and AER with those from ALL forcing simulations, we find the traditional detection and attribution approaches based on a single AER mode might produce biased results, especially as AER's second mode becomes increasingly dominant over time and resembles the GHG response pattern.

While our analysis has focused on the past century, the results and conclusions may change for future forcing scenarios. As global AER emissions are projected to decrease with clean-air efforts, AER PC1 will likely change sign in the future. Given the anti-correlation between AER PC1 and GHG PC1, the future AER effect may exacerbate GHG-induced climate change and enhance its detectability. Hence, it remains to be further investigated how our proposed framework will evolve in the future, accounting for various uncertainties arising from model structures, emission scenarios, and representations of AER (direct and indirect) forcings.

Data Availability Statement

The study used the CESM1 Large Ensemble data (Kay et al., 2015a, 2015b) and single-forcing large ensemble data (Deser et al., 2020a, 2020b). Code to perform LFCA (Wills et al., 2018a) is available on Github https://github.com/rcjwills/lfca (Wills et al., 2018b).

References

Ackerman, A. S., Kirkpatrick, M. P., Stevens, D. E., & Toon, O. B. (2004). The impact of humidity above stratiform clouds on indirect aerosol climate forcing. *Nature*, *432*(7020), 1014–1017. https://doi.org/10.1038/nature03174

Bonfils, C. J., Santer, B. D., Fyfe, J. C., Marvel, K., Phillips, T. J., & Zimmerman, S. R. (2020). Human influence on joint changes in temperature, rainfall and continental aridity. *Nature Climate Change*, *10*(8), 726–731. https://doi.org/10.1038/s41558-020-0821-1

Capotondi, A., Alexander, M. A., Bond, N. A., Curchitser, E. N., & Scott, J. D. (2012). Enhanced upper ocean stratification with climate change in the CMIP3 models. *Journal of Geophysical Research*, *117*(C4). https://doi.org/10.1029/2011jc007409

Deser, C., Phillips, A. S., Simpson, I. R., Rosenbloom, N., Coleman, D., Lehner, F., et al. (2020a). Isolating the evolving contributions of anthropogenic aerosols and greenhouse gases: A new CESM1 large ensemble community resource. *Journal of Climate*, *33*(18), 7835–7858. https://doi.org/10.1175/jcli-d-20-0123.1

Deser, C., Phillips, A. S., Simpson, I. R., Rosenbloom, N., Coleman, D., Lehner, F., et al. (2020b). CESM1 single forcing large ensemble project [dataset]. *Climate Data Gateway at NCAR*. https://www.cesm.ucar.edu/working-groups/climate/simulations/cesm1-single-forcing-le/

Dittus, A. J., Hawkins, E., Robson, J. I., Smith, D. M., & Wilcox, L. J. (2021). Drivers of recent North Pacific decadal variability: The role of aerosol forcing. *Earth's Future*, *9*(12), e2021EF002249. https://doi.org/10.1029/2021ef002249

Dong, H., Song, F., Liu, F., Wang, H., Dong, L., Leung, L. R., & Lu, J. (2024). Seasonal delay of sahelian rainfall driven by an east–west contrast in radiative forcing in idealized CESM experiments. *Climate Dynamics*, *62*(11), 1–18. https://doi.org/10.1007/s00382-024-07452-3

Dörr, J. S., Bonan, D. B., Årthun, M., Svendsen, L., & Wills, R. C. (2023). Forced and internal components of observed Arctic sea-ice changes. *The Cryosphere Discussions*, *2023*(9), 1–27. https://doi.org/10.5194/tc-17-4133-2023

Durack, P. J., Wijffels, S. E., & Matear, R. J. (2012). Ocean salinities reveal strong global water cycle intensification during 1950 to 2000. *Science*, *336*(6080), 455–458. https://doi.org/10.1126/science.1212222

Forster, P., Storelvmo, T., Armour, K., Collins, W., Dufresne, J.-L., & Frame, D. (2021). The earth's energy budget, climate feedbacks, and climate sensitivity.

Held, I. M., & Soden, B. J. (2006). Robust responses of the hydrological cycle to global warming. *Journal of Climate*, *19*(21), 5686–5699. https://doi.org/10.1175/jcli3990.1

Hwang, Y.-T., Frierson, D. M., & Kang, S. M. (2013). Anthropogenic sulfate aerosol and the southward shift of tropical precipitation in the late 20th century. *Geophysical Research Letters*, *40*(11), 2845–2850. https://doi.org/10.1002/grl.50502

Kang, S. M., Held, I. M., Frierson, D. M., & Zhao, M. (2008). The response of the ITCZ to extratropical thermal forcing: Idealized slab-ocean experiments with a GCM. *Journal of Climate*, *21*(14), 3521–3532. https://doi.org/10.1175/2007jcli2146.1

Kang, S. M., Xie, S.-P., Deser, C., & Xiang, B. (2021). Zonal mean and shift modes of historical climate response to evolving aerosol distribution. *Science Bulletin*, *66*(23), 2405–2411. https://doi.org/10.1016/j.scib.2021.07.013

Kay, J. E., Deser, C., Phillips, A., Mai, A., Hannay, C., & Strand, G. (2015). Large ensemble community project (LENS) [dataset]. *Climate Data Gateway at NCAR*. https://www.cesm.ucar.edu/community-projects/lens/data-sets/

Kay, J. E., Deser, C., Phillips, A., Mai, A., Hannay, C., Strand, G., et al. (2015). The community earth system model (CESM) large ensemble project: A community resource for studying climate change in the presence of internal climate variability. *Bulletin of the American Meteorological Society*, *96*(8), 1333–1349. https://doi.org/10.1175/bams-d-13-00255.1

Kuo, Y.-N., Kim, H., & Lehner, F. (2023). Anthropogenic aerosols contribute to the recent decline in precipitation over the US Southwest. *Geophysical Research Letters*, *50*(23), e2023GL105389. https://doi.org/10.1029/2023gl105389

Menary, M. B., Robson, J., Allan, R. P., Booth, B. B., Cassou, C., Gastineau, G., et al. (2020). Aerosol-forced AMOC changes in cmip6 historical simulations. *Geophysical Research Letters*, *47*(14), e2020GL088166. https://doi.org/10.1029/2020gl088166

Myhre, G., Shindell, D., Bréon, F.-M., Collins, W., Fuglestvedt, J., & Huang, J. (2014). Anthropogenic and natural radiative forcing. *Climate Change 2013-The Physical Science Basis*, 659–740.

Shi, J.-R., Kwon, Y.-O., & Wijffels, S. E. (2022). Two distinct modes of climate responses to the anthropogenic aerosol forcing changes. *Journal of Climate*, *35*(11), 3445–3457. https://doi.org/10.1175/jcli-d-21-0656.1

Smith, D. M., Booth, B. B., Dunstone, N. J., Eade, R., Hermanson, L., Jones, G. S., et al. (2016). Role of volcanic and anthropogenic aerosols in the recent global surface warming slowdown. *Nature Climate Change*, *6*(10), 936–940. https://doi.org/10.1038/nclimate3058

Song, F., Leung, L. R., Lu, J., Dong, L., Zhou, W., Harrop, B., & Qian, Y. (2021). Emergence of seasonal delay of tropical rainfall during 1979–2019. *Nature Climate Change*, *11*(7), 605–612. https://doi.org/10.1038/s41558-021-01066-x

Sun, Q., Du, Y., Xie, S.-P., Zhang, Y., Wang, M., & Kosaka, Y. (2021). Sea surface salinity change since 1950: Internal variability versus anthropogenic forcing. *Journal of Climate*, *34*(4), 1305–1319. https://doi.org/10.1175/jcli-d-20-0331.1

Twomey, S. (1977). Atmospheric aerosols.

Wang, H., & Wen, Y.-J. (2022). Climate response to the spatial and temporal evolutions of anthropogenic aerosol forcing. *Climate Dynamics*, *59*(5), 1579–1595. https://doi.org/10.1007/s00382-021-06059-2

Wang, H., Xie, S.-P., & Liu, Q. (2016). Comparison of climate response to anthropogenic aerosol versus greenhouse gas forcing: Distinct patterns. *Journal of Climate*, *29*(14), 5175–5188. https://doi.org/10.1175/jcli-d-16-0106.1

Wills, R. C., Dong, Y., Proistosecu, C., Armour, K. C., & Battisti, D. S. (2022). Systematic climate model biases in the large-scale patterns of recent sea-surface temperature and sea-level pressure change. *Geophysical Research Letters*, *49*(17), e2022GL100011. https://doi.org/10.1029/2022gl100011

Wills, R. C., Schneider, T., Wallace, J. M., Battisti, D. S., & Hartmann, D. L. (2018a). Disentangling global warming, multidecadal variability, and El niño in Pacific temperatures. *Geophysical Research Letters*, *45*(5), 2487–2496. https://doi.org/10.1002/2017gl076327

Wills, R. C., Schneider, T., Wallace, J. M., Battisti, D. S., & Hartmann, D. L. (2018b). Lfca [SOFTWARE]. *Github*. https://github.com/rcjwills/lfca/

Xie, S.-P., Deser, C., Vecchi, G. A., Ma, J., Teng, H., & Wittenberg, A. T. (2010). Global warming pattern formation: Sea surface temperature and rainfall. *Journal of Climate*, *23*(4), 966–986. https://doi.org/10.1175/2009jcli3329.1

Xie, S.-P., Lu, B., & Xiang, B. (2013). Similar spatial patterns of climate responses to aerosol and greenhouse gas changes. *Nature Geoscience*, *6*(10), 828–832. https://doi.org/10.1038/ngeo1931